Supplementary Materials

Table S1. Major element oxides in the constituents used to prepare the cement pastes (n.a.: not analysed) (Isaacs et al., 2020 [44]).

| Material	CaO (wt.%)	SiO$_2$ (wt.%)	Al$_2$O$_3$ (wt.%)	MgO (wt.%)	K$_2$O (wt.%)	Fe$_2$O$_3$ (wt.%)	MnO (wt.%)	TiO$_2$ (wt.%)	SO$_3$ (wt.%)	P$_2$O$_5$ (wt.%)
CEM I [a]	66.27	17.86	4.78	2.75	1.52	2.65	n.a.	0.2	3.98	n.a.
PFA [b]	3.86	48.66	25.97	1.27	5.05	12.36	n.a.	0.84	1.82	0.18
GGBS [c]	42.93	31.92	11.40	6.76	1.01	0.45	0.59	0.41	4.10	n.a.
Hydrated Lime [d]	97.75	1.37	0.35	0.20	0.33	n.a.	n.a.	n.a.	n.a.	n.a.
Lime Flour [e]	96.57	1.70	0.71	0.29	0.39	0.16	n.a.	n.a.	0.18	n.a.
CEM I (VTT) [f]	67.72	17.60	3.42	0.60	1.30	5.17	0.21	0.17	3.81	n.a.
GGBS (VTT) [g]	43.13	32.3	9.85	7.40	1.20	0.74	0.34	1.36	3.68	n.a.
Silica Fume (VTT) [g]	1.46	93.10	1.44	0.88	1.73	0.91	n.a.	n.a.	0.47	n.a.

[a] CEM I 42.5N, Hanson Cement, Ribblesdale, UK; [b] source unknown; [c] Hanson Cement, Scunthorpe, UK; [d] Lafarge Cement, UK; [e] NAF, Monmouth, UK; [f] Cementa, Finland; [g] Finnsementti, Finland.

Table S2. Composition of aqueous solutions equilibrated with HCP used in batch sorption and through diffusion experiments (-: below detection limit) (Isaacs et al., 2020 [44]).

Binder	pH (-)	Eh (mV)	Na (mg kg^{-1})	K (mg kg^{-1})	Ca (mg kg^{-1})	Mg (mg kg^{-1})	Cl (mg kg^{-1})	SO$_4$ (mg kg^{-1})	NO$_3$ (mg kg^{-1})
CEM I	12.8	-14	267.6	453.3	1388.4	-	18.0	36.9	18.1
PFA–OPC	12.3	-503	129.8	195.2	675.8	39.0	14.4	31.0	16.3
GGBS–OPC	12.8	-414	68.6	70.2	299.6	-	16.9	34.7	17.6
NRVB	12.9	-129	172.5	224.7	1374.3	66.3	16.0	33.6	17.2
Cebama	12.7	-454	189.7	202.3	1046.6	137.0	24.0	50.3	20.4

Table S3. pH of aqueous solutions equilibrated with synthesised cement hydration phases (Lange, 2019 [34]).

Hydration phase	C-S-H 0.9	AFm-SO$_4$	AFm-CO$_3$
pH (-)	11.9 ± 0.2	12.0 ± 0.2	11.3 ± 0.2
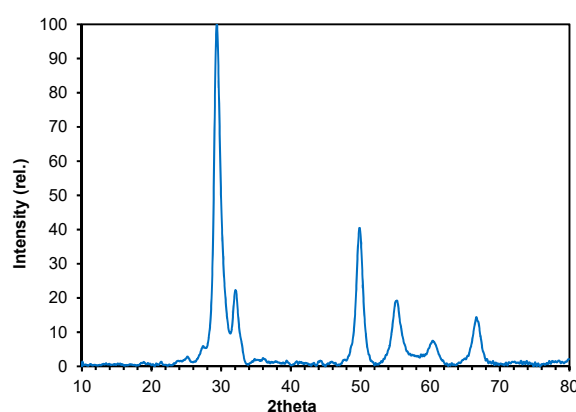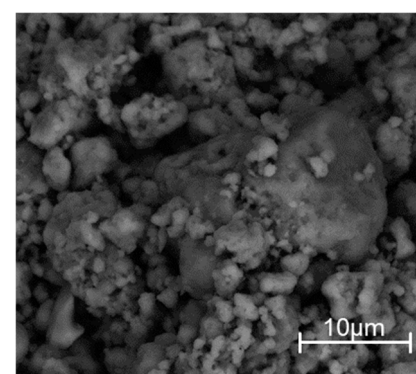
(a) (b)

Figure S1. (a) XRD pattern of C-S-H0.9 and (**b**) SEM image (back-scattered electron mode) of C-S-H0.9 (Lange, 2019 [34]). The XRD pattern reveals only reflexes typical for C-S-H; no reflexes corresponding to portlandite were found, indicating that potentially occurring portlandite impurities were below 1 wt.%. In the SEM image, C-S-H0.9 exhibits the typical fine-grained cloudy microstructure, corresponding to its nanocrystalline nature.
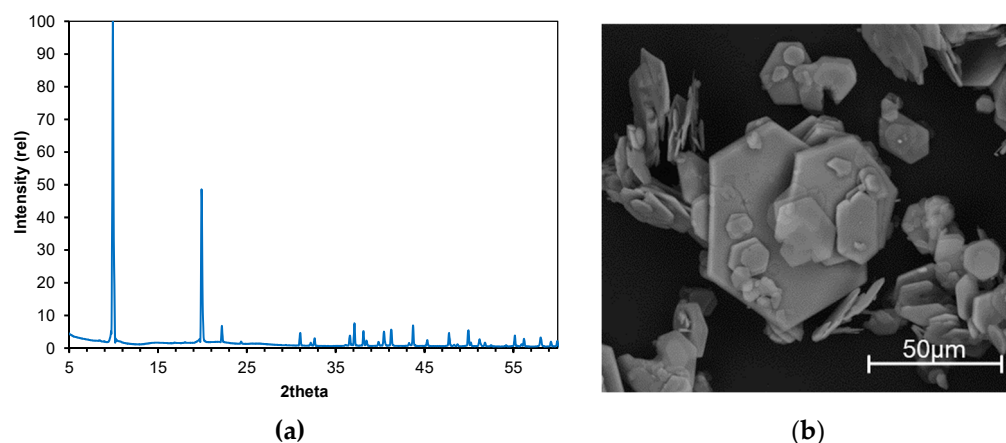
(a)

(b)

Figure S2. (**a**) XRD pattern of AFm-SO$_4$ and (**b**) SEM image (back-scattered electron mode) of AFm-SO$_4$ (Lange, 2019 [34]). The XRD pattern indicates synthesis of pure monosulphoaluminate hydrate and preferential orientation of the sheet-like material with a strong reflex for the basal spacing (0 0 3) at 9.9° 2θ. The SEM image shows well-developed idiomorphic AFm-SO$_4$ platelets.
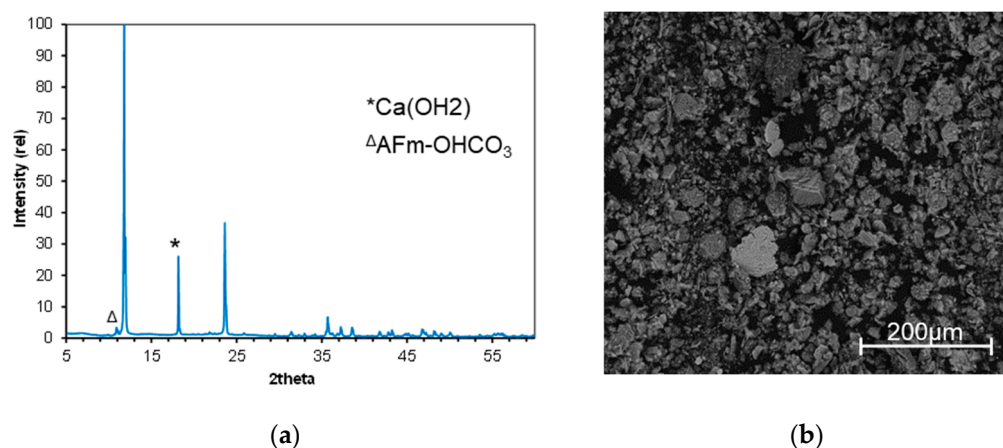

*Ca(OH2)
△AFm-OHCO$_3$

(a)

(b)

Figure S3. (**a**) XRD pattern of AFm-CO$_3$ and (**b**) SEM image (back-scattered electron mode) of AFm-CO$_3$ (Lange, 2019 [34]). The XRD pattern indicates preferential orientation of the sheet-like AFm with a strong reflex for the basal spacing (0 0 3) at 11.7° 2θ. Reflexes at 10.8° 2θ and 18° 2θ indicate the presence of minor amounts of hemicarbonate (AFm-OHCO$_3$; $Ca_4Al_2(OH)_{12}(CO_3)_{0.5}OH \cdot 6H_2O$) and portlandite, respectively. The SEM image reveals a significantly lower grain size and only poorly developed crystals compared to the AFm-SO$_4$.